THE ASTROPHYSICAL JOURNAL, 812:105 (9pp), 2015 October 20 doi:10.1088/0004-637X/812/2/105


# ELECTRIC CURRENT FILAMENTATION AT A NON-POTENTIAL MAGNETIC NULL-POINT DUE TO PRESSURE PERTURBATION

P. JELÍNEK[1], M. KARLICKÝ[2], AND K. MURAWSKI[3]
[1] University of South Bohemia, Faculty of Science, Institute of Physics and Biophysics, Branišovská 10, CZ-37005 České Budějovice, Czech Republic; pjelinek@prf.jcu.cz
[2] Academy of Sciences of the Czech Republic, v. v. i., Astronomical Institute, Fričova 258, CZ-25165 Ondřejov, Czech Republic
[3] Maria Curie-Skłodowska University, Institute of Physics, Group of Astrophysics, Radziszewskiego 10, PL-20031 Lublin, Poland
*Received 2015 June 19; accepted 2015 September 11; published 2015 October 13*

## ABSTRACT

An increase of electric current densities due to filamentation is an important process in any flare. We show that the pressure perturbation, followed by an entropy wave, triggers such a filamentation in the non-potential magnetic null-point. In the two-dimensional (2D), non-potential magnetic null-point, we generate the entropy wave by a negative or positive pressure pulse that is launched initially. Then, we study its evolution under the influence of the gravity field. We solve the full set of 2D time dependent, ideal magnetohydrodynamic equations numerically, making use of the FLASH code. The negative pulse leads to an entropy wave with a plasma density greater than in the ambient atmosphere and thus this wave falls down in the solar atmosphere, attracted by the gravity force. In the case of the positive pressure pulse, the plasma becomes evacuated and the entropy wave propagates upward. However, in both cases, owing to the Rayleigh–Taylor instability, the electric current in a non-potential magnetic null-point is rapidly filamented and at some locations the electric current density is strongly enhanced in comparison to its initial value. Using numerical simulations, we find that entropy waves initiated either by positive or negative pulses result in an increase of electric current densities close to the magnetic null-point and thus the energy accumulated here can be released as nanoflares or even flares.

*Key words:* magnetohydrodynamics (MHD) – methods: numerical – Sun: corona – Sun: flares – waves

## 1. INTRODUCTION

Magnetohydrodynamic (MHD) waves are omnipresent in the solar atmosphere. Their study is one of the most rapidly developing branches of solar physics; see the recent review by De Moortel & Nakariakov (2012). The diversity of MHD waves is studied in various structures, e.g., in simple density slabs and Harris current-sheets (Jelínek & Karlický 2012; Jelínek et al. 2012; Mészárosová et al. 2014), and in magnetic funnels and open magnetic structures (Jelínek & Murawski 2013; Pascoe et al. 2013, 2014). Recent numerical results are summarized by Pascoe (2014) and are also confirmed by observations, e.g., by Nisticò et al. (2013, 2014).

Among these MHD waves is the so-called entropy wave, (Goedbloed & Poedts 2004). Similarly to slow and fast MHD waves, the entropy wave is the solution for the dispersion relation in MHD equations. In this wave, the plasma velocity, magnetic field, and gas pressure remain undisturbed. The only disturbed quantities are the plasma density, and, as a result of that, the temperature and entropy. In a still and gravity-free medium, this wave is non-propagating, i.e., the phase-velocity (or frequency) of this wave is zero with respect to the medium. In the case of non-ideal plasma, the entropy wave has an equivalent, which is called the thermal mode (Field 1965; De Moortel & Hood 2003; Macnamara & Roberts 2010). This wave has been considered in the problem of reconnecting current sheets; see Somov (2012) and references therein. However, this wave is generally believed to be rapidly damped (De Moortel & Hood 2003; Murawski et al. 2011) and usually neglected (Somov 2012). However, in the paper by Murawski et al. (2011) it was proposed that the entropy wave at magnetic null-points can consist of indirect observational evidence of nanoflares in the solar corona. In the present paper, we follow this idea, and instead of the potential magnetic null-point studied by Murawski et al. (2011), we consider the more general case of the non-potential magnetic null-point. In such a null-point, there is a free energy that can be released in the form of nanoflares or even flares. Similarly to the paper by Murawski et al. (2011) we assume that the entropy wave is generated by a sudden pressure pulse: (a) the negative pressure pulse that may result from the thermal instability or (b) the positive pressure pulse that mimics thermal energy release.

In this paper, we show that during an evolution of the entropy wave in the non-potential null-point the electric current is rapidly filamentated and at some locations the current densities are strongly enhanced. The filamentation of the electric current is an essential process in any flare as is shown by, e.g., Bárta et al. (2011) and Nickeler et al. (2013). At locations with the enhanced electric current densities, when their values become greater than the thresholds for some plasma instabilities (e.g., the ion-sound or Buneman instability), plasma waves can be generated and the anomalous resistivity is produced (Foullon et al. 2005; Nakariakov et al. 2006). These processes release the magnetic field energy through Ohmic dissipation.

This paper is structured as follows. In Section 2, we describe our numerical model with the initial equilibrium and perturbations implemented. The results of numerical simulations and their interpretation are summarized in Section 3. Finally, we complete the paper by concluding in Section 4.

## 2. MODEL

In this section, we describe physical and numerical models of the null-point and adopt them to study entropy waves that are triggered by pressure pulses that are launched at the null-point.

### 2.1. Governing Equations

Our numerical model describes the gravitationally stratified solar atmosphere, in which the plasma dynamics is described by the two-dimensional (2D), time-dependent, ideal MHD equations (see, e.g., Priest 1982; Chung 2002):

$$\frac{D\varrho}{Dt} = -\varrho\nabla\boldsymbol{v}, \quad (1)$$

$$\varrho\frac{D\boldsymbol{v}}{Dt} = -\nabla p + \boldsymbol{j} \times \boldsymbol{B} + \varrho\boldsymbol{g}, \quad (2)$$

$$\frac{D}{Dt}\left(\frac{\boldsymbol{B}}{\varrho}\right) = \left(\frac{\boldsymbol{B}}{\varrho}\cdot\nabla\right)\boldsymbol{v}, \quad (3)$$

$$\frac{D(\varrho U)}{Dt} = -\varrho U(\gamma - 1)\nabla\cdot\boldsymbol{v}, \quad (4)$$

$$\nabla\cdot\boldsymbol{B} = 0. \quad (5)$$

Here $D/Dt \equiv \partial/\partial t + \boldsymbol{v}\cdot\nabla$ is the material (or convective) time derivative, $\varrho$ is a mass density, $\boldsymbol{v}$ flow velocity, $\boldsymbol{B}$ the magnetic field, $\boldsymbol{g} = [0, -g_\odot, 0]$ the gravitational acceleration with $g_\odot = 274$ m s$^{-2}$, and the adiabatic coefficient $\gamma = 5/3$. Current density $\boldsymbol{j}$ in Equation (2) is expressed as

$$\boldsymbol{j} = \frac{1}{\mu_0}\nabla\times\boldsymbol{B}, \quad (6)$$

where $\mu_0 = 1.26 \times 10^{-6}$ H m$^{-1}$ is the magnetic permeability of free space. The specific internal energy, $U$, in Equation (4) is given by

$$U = \frac{p}{(\gamma - 1)\varrho}. \quad (7)$$

Similarly to Murawski et al. (2011), we neglect the radiative losses and thermal conduction.

### 2.2. Initial Equilibrium

For a still ($\boldsymbol{v} = 0$) equilibrium, the Lorentz and gravity forces have to be balanced by the pressure gradient in the entire physical domain,

$$-\nabla p + \boldsymbol{j}\times\boldsymbol{B} + \varrho\boldsymbol{g} = \boldsymbol{0}. \quad (8)$$

Assuming a force-free magnetic field, $\boldsymbol{j}\times\boldsymbol{B} = 0$, in the null-point, the solution of the remaining hydrostatic equation yields

$$p_{\rm h}(y) = p_0 \exp\left[-\int_{y_0}^{y}\frac{1}{\Lambda(\tilde{y})}d\tilde{y}\right], \quad (9)$$

$$\varrho(y) = \frac{p(y)}{g_\odot\Lambda(y)}. \quad (10)$$

Here

$$\Lambda(y) = \frac{k_{\rm B}T(y)}{\overline{m}g_\odot} \quad (11)$$

is the pressure scale-height, which, in the case of isothermal atmosphere, represents the vertical distance over which the gas pressure decreases by a factor of $e \approx 2.7$, $k_{\rm B} = 1.38 \times 10^{-23}$ J K$^{-1}$ is the Boltzmann constant and $\overline{m} = 0.6\, m_{\rm p}$ is the mean particle mass ($m_{\rm p} = 1.672 \times 10^{-27}$ kg is the proton mass), and $p_0 \approx 10^{-2}$ Pa in Equation (9) denotes the gas pressure at the reference level $y_0$. In our calculations, we set and hold fixed at $y_0 = 10$ Mm.

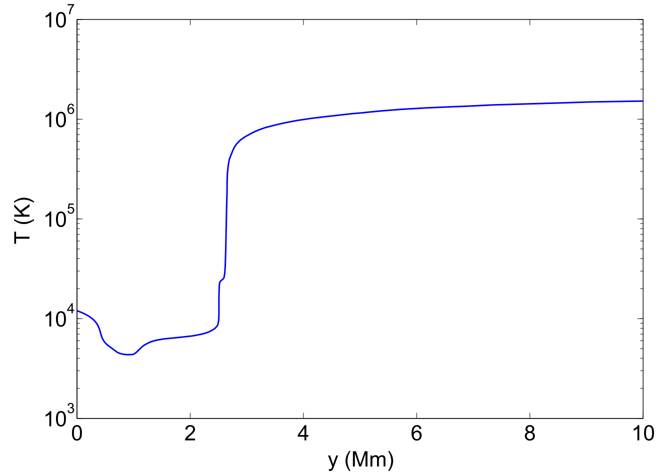


**Figure 1.** Temperature profile, $T(y)$, in logarithmic scale as a function of height $y$ in the solar atmosphere.

For the solar atmosphere, the temperature profile $T(y)$ (see Figure 1) was derived by Vernazza et al. (1981). At the top of the photosphere, which corresponds to the height $y = 0.5$ Mm, and the temperature is $T(y) = 5700$ K. At higher altitudes, the temperature falls down to its minimal value $T(y) = 4350$ K at $y \approx 0.95$ Mm. Higher up, the temperature rises slowly to the height of about $y = 2.7$ Mm, where the transition region is located. Here the temperature grows up abruptly to the value, $T(y) = 1.5$ MK, at the altitude $y = 10$ Mm, which is typical for the solar corona.

The solenoidal condition, $\nabla\cdot\boldsymbol{B} = 0$, is identically satisfied with the use of the magnetic flux function, $\boldsymbol{A}$, such as

$$\boldsymbol{B} = \nabla\times\boldsymbol{A}. \quad (12)$$

Specifically, to represent the non-potential null-point, we use

$$\boldsymbol{A} = [0, 0, A_z]$$

with (Parnell et al. 1997)

$$A_z = \frac{1}{4}B_0\left[(\mathcal{J}_t - \mathcal{J}_z)y^2 - (\mathcal{J}_t + \mathcal{J}_z)x^2\right], \quad (13)$$

where $\mathcal{J}_t$ is the threshold current, which only depends on the parameters associated with the potential part of the field and it is assumed to be a constant in our calculations. The parameter $\mathcal{J}_z$ is the magnitude of the current perpendicular to the plane of the null-point. Both $\mathcal{J}_t$ and $\mathcal{J}_z$ are free parameters that govern the magnetic field configuration. For $\mathcal{J}_z = 0$, we get a potential null-point, for $|\mathcal{J}_z| < \mathcal{J}_t$ a non-potential null-point, anti-parallel magnetic field lines $|\mathcal{J}_z| = \mathcal{J}_t$, and an elliptical null for $|\mathcal{J}_z| > \mathcal{J}_t$. See Parnell et al. (1997) for more details. The magnetic field at the reference level is set and held fixed as $B_0 = 10$ G.

The equilibrium gas pressure and mass density are computed according to the following equations; see, e.g., Solov'ev (2010) and Kuźma et al. (2015):

$$p(x, y) = p_{\rm h} - \frac{1}{\mu_0}\left[\int_{-\infty}^{x}\frac{\partial^2 A}{\partial y^2}\frac{\partial A}{\partial x}dx + \frac{1}{2}\left(\frac{\partial A}{\partial x}\right)^2\right], \quad (14)$$

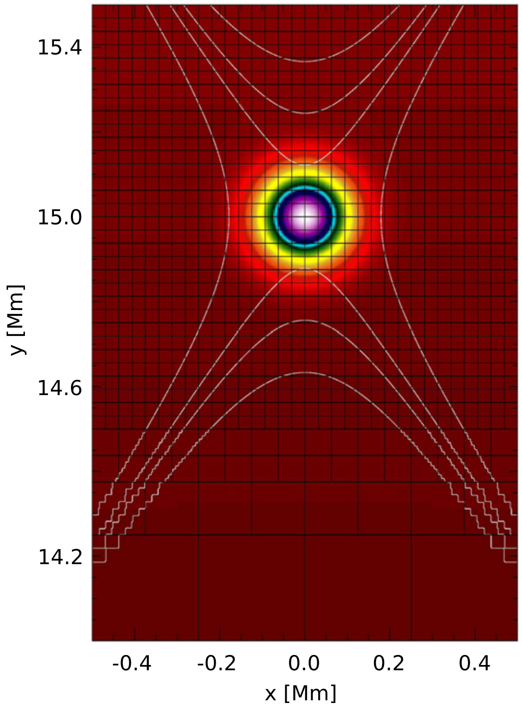


**Figure 2.** Simulation region for the negative pressure pulse ($A_p = -0.75$) launched in the center of the magnetic null-point. The white solid lines represent magnetic field lines which the typical X-shape in the center. As a complement, the computational blocks are also shown by thin, black, solid boxes.

$$\varrho(x, y) = \varrho_{\rm h}(y) + \frac{1}{\mu_0 g_\odot}\left\{\frac{\partial}{\partial y}\left[\int_{-\infty}^{x}\frac{\partial^2 A}{\partial y^2}\frac{\partial A}{\partial x}dx + \frac{1}{2}\left(\frac{\partial A}{\partial x}\right)^2\right] - \frac{\partial A}{\partial y}\nabla^2 A\right\}. \quad (15)$$

With the use of Equation (13) in these general formulas, we obtain the expressions for the equilibrium gas pressure

$$p(x, y) = p_{\rm h}(y) - \frac{B_0^2}{4\mu_0}\mathcal{J}_z(\mathcal{J}_t + \mathcal{J}_z)x^2 \quad (16)$$

and mass density

$$\varrho(x, y) = \varrho_{\rm h}(y) + \frac{B_0^2}{2\mu_0 g}\mathcal{J}_z(\mathcal{J}_t - \mathcal{J}_z)y. \quad (17)$$

### 2.3. Perturbations

At the start of the numerical simulation ($t = 0$ s), the equilibrium with the magnetic null-point is perturbed, similarly to Murawski et al. (2011), by a Gaussian pulse of the following form:

$$p(x, y, t = 0) = p_0\left\{1 + A_{\rm p}\exp\left[-\frac{x^2 + (y - y_{\rm P})^2}{w^2}\right]\right\}, \quad (18)$$

where $p_0$ is the initial gas pressure, $A_p$ denotes the initial amplitude of the pulse, $y_{\rm P} = 15$ Mm is the position of the perturbation point, and $w = 0.1$ Mm is the width of the pressure pulse; see Figure 2. The negative pressure pulse corresponds to $A_p < 0$ and it mimics plasma cooling, while the pressure pulse is represented by $A_p > 0$ and it indicates plasma heating, which is implemented near the magnetic null-point. Note that, despite the negative pressure pulse, the total pressure $p(x, y, t = 0)$ in Equation (18) remains positive.

### 2.4. Numerical Code

We solve the 2D time-dependent, ideal MHD Equations (1)–(4) numerically, making use of the FLASH code (Fryxell et al. 2000; Lee & Deane 2009). It is now a well tested, fully modular, parallel, multi-physics, open science, simulation code that implements second- and third-order unsplit Godunov solvers with various slope limiters and Riemann solvers as well as adaptive mesh refinement (AMR; e.g., Chung 2002). The Godunov solver combines the corner transport upwind method for multi-dimensional integration and the constrained transport algorithm for preserving the divergence-free constraint on the magnetic field (Lee & Deane 2009). We use the minmod slope limiter and the Riemann solver (e.g., Toro 2006). The main advantage of using the AMR technique is to refine a numerical grid at steep spatial profiles while keeping the grid coarse at the places where fine spatial resolution is not essential. In our case, the AMR strategy is based on controlling the numerical errors in a gradient of mass density that leads to the reduction of the numerical diffusion within the entire simulation region.

For our numerical simulations, we use a 2D Eulerian box of its height $H = 2$ Mm; see Figure 2. Note that in this figure the simulation region is zoomed in to display the null-point including the initial perturbation in more detail. The spatial resolution of the numerical grid is determined by the AMR method. We use the AMR grid with the minimum (maximum) level of the refinement blocks set to 3 (6). The whole simulation region is covered by 1434 blocks. Since every block consists of $8 \times 8$ numerical cells, this number of blocks corresponds to 91,776 numerical cells, and the smallest spatial resolution is $\Delta x = \Delta y = 3.9$ km.

At all boundaries, we fix all plasma quantities to their equilibrium values, which lead only to negligibly small numerical reflections of incident wave signals.

## 3. NUMERICAL RESULTS

Prior to performing numerical simulations, by making the simulation test, we verify that for the adopted grid resolution the system remains in numerical equilibrium, while not being perturbed by any gas pressure pulse. After this basic numerical test, we start to simulate the system dynamics by launching either negative and positive initial gas pressure pulses. Because we study the non-potential magnetic neutral point, we assume in all considered cases that ($|\mathcal{J}_z| < \mathcal{J}_t$); see Parnell et al. (1997). We perform numerical simulations for the following cases: (a) $\mathcal{J}_t/\mathcal{J}_z = 1.25$; (b) $\mathcal{J}_t/\mathcal{J}_z = 2.5$; (c) $\mathcal{J}_t/\mathcal{J}_z = 5.0$. However, we show here the preferential results for $\mathcal{J}_t/\mathcal{J}_z = 2.5$, while the results for cases (a) and (c) are simply compared with those obtained for case (b).

### 3.1. Null-point with the Negative Pressure Pulse

We assume here the negative amplitude of the initial pressure pulse, $A_p = -0.75$. In Figure 3, we present the evolution of the mass density. At $t = 1$ s, we see that the initial pressure pulse triggered fast and slow magnetoacoustic waves

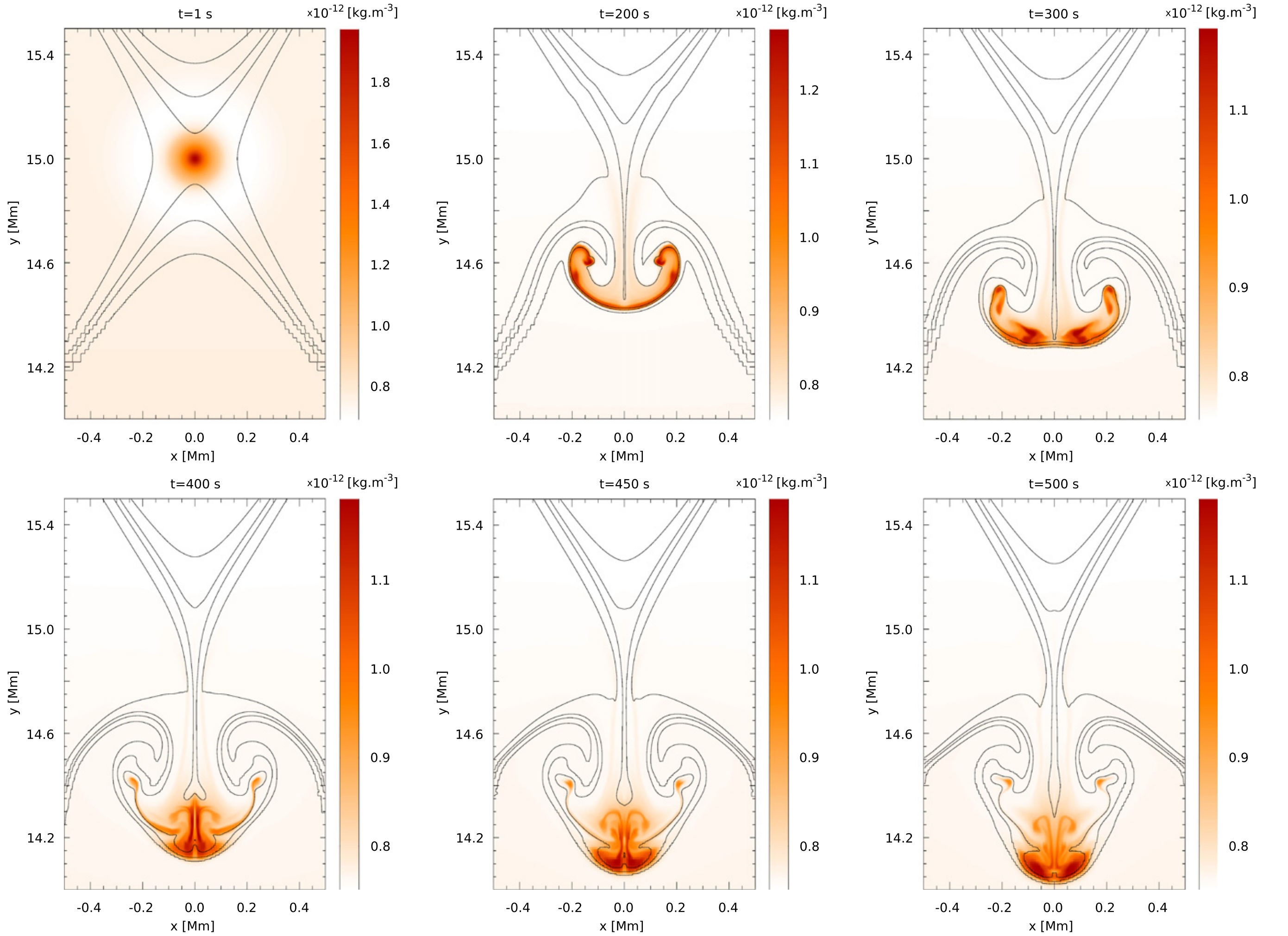


**Figure 3.** Time evolution of mass density for $A_p = -0.75$, with a clear development of Rayleigh–Taylor instability. The black solid lines show representative magnetic field lines.

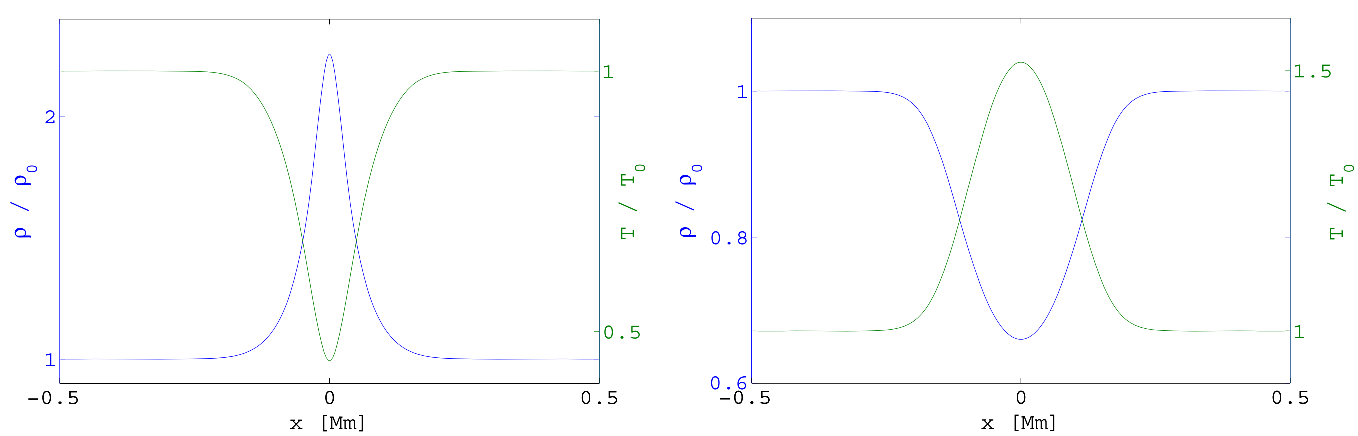


**Figure 4.** Entropy mode at $t = 10$ s, represented by rarefied and hot plasma regions in the case of the negative initial pressure pulse (left panel) and the positive pressure pulse (right panel).

that propagate quasi-isotropically out of the null-point (see the expanding circular feature at $t = 1$ s).

Later on, as a result of the initial negative pressure pulse, the entropy wave with the enhanced mass density and decreased temperature is formed; see their profiles in Figure 4, left panel. Very shortly after the initial pressure pulse ($\approx$15 s), the entropy wave, represented by the dense blob, starts to move down, along the direction of the gravity action force. Because this blob falls down to an environment with higher density, after some time ($\approx$100–150 s) the Rayleigh–Taylor (RT) instability develops. At $t \approx 350$ s, the blob starts to move up because it is reflected from high density layers and also due to the action of magnetic tension force, and then at $t \approx 400$ s it moves down again.

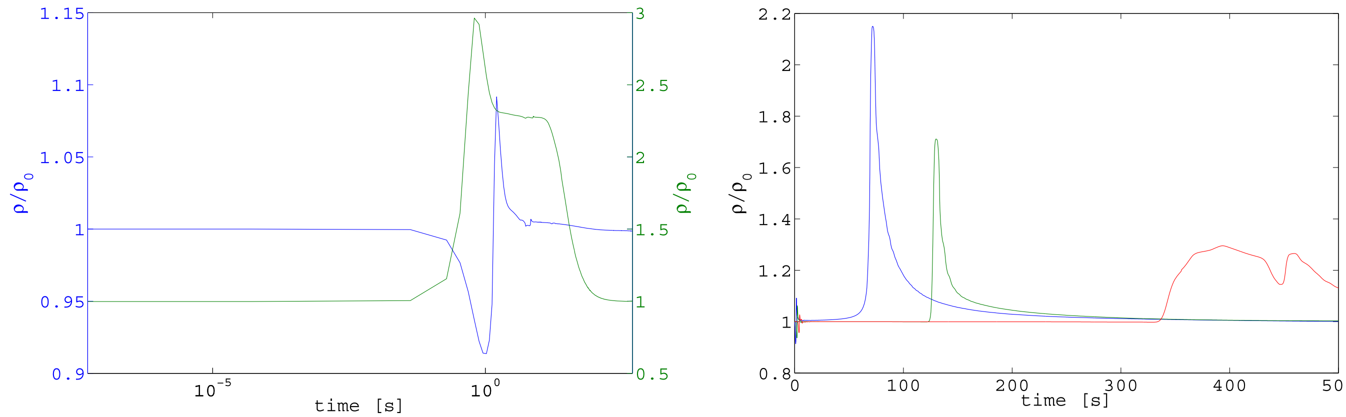


**Figure 5.** Time evolution of mass density in the case of $A_p = -0.75$, collected at the detection points placed at $x = 0$ Mm along the $y$ axis in positions $y = 15.2$ Mm (left blue line) and $y = 15.0$ Mm (left green line) and $y = 14.8$, $y = 14.6$, and $y = 14.2$ Mm (right red, green, and blue line, respectively). Note that the time axis on the left-hand side is in the logarithmic scale, showing the very beginning of the process.

In Figure 5, we present the time evolution of the mass density computed at different detection points. In the left panel, we show the mass density in two detection points ((0, 15.2) Mm (blue) and (0, 15.0) Mm (green)). The initial pressure pulse triggers large amplitude magnetoacoustic waves. After the initial phase which lasts until $t \approx 10$ s, and during which fast and slow magnetoacoustic waves pass the detection point, the mass density starts to saturate slowly to its equilibrium value (Figure 5, left panel, blue line). This fits the theory of entropy waves perfectly, according to which the entropy waves affect the mass density; for a negative pressure pulse, the mass density $\varrho$ should increase as is indeed observed in the numerical experiments.

In the right panel of Figure 5, we see the evolution of the mass density in three detection points located below the perturbation point ($y = 14.8$, $y = 14.6$, and $y = 14.2$ Mm, red, green, and blue colored lines, respectively). At the very beginning (within the order of seconds) we can again observe the propagating fast magnetoacoustic waves. After the passage of magnetoacoustic waves, the system slowly relaxes to its equilibrium state followed, after some time, by a steep increase in mass density, depending on the position of a detection point. Because the blob descends to the denser layers of the solar atmosphere, the amplitude of these waves decreases, which is clearly seen by comparing all of the lines in this plot. Furthermore, the blue line shows how the blob is reflected from layers at lower altitudes with higher densities.

Figure 6 consists of four panels. The upper left panel shows the current density distribution at time $t^{\max} = 242$ s, i.e., at the time when its maximum value has been reached. From this figure, one can see that the maximum value of the current density is located in the vicinity of the vertical axis of the null-point. As the mass density at this time slowly relaxes to the equilibrium value (see Figure 5 right part), the electron velocity, according to the relation for electric current density, $\boldsymbol{j} = -ne\boldsymbol{v}$, attains its maximum as well.

In the upper right panel of Figure 6, we present the time evolution of the maximal current density detected along the vertical axis of the null point. Note that the vertical axis is in logarithmic scale to show the time evolution in more detail. In this figure, there are two maxima. The first one appears very shortly after the initial perturbation (units of seconds). This is very likely related to the rapid increase of mass density in the null-point. Then, the current density rapidly decreases simultaneously with the mass density decrease. After ≈10–15 s, the current density starts to grow slowly again, but now as the result of the electron velocity increase.

Finally, the two bottom panels of Figure 6 illustrate the horizontal (left) and vertical slices (right) of the current density. The horizontal slice is taken at the point of the maximal value of the electric current density, i.e., at ($x = \langle -0.5, 0.5\rangle$ and $y = 14.65$). The vertical slice is displayed along the axis of the null-point, i.e., at ($x = 0$ and $y = \langle 13.5, 15.5\rangle$). From both of these panels and also from the upper right panel, we can find that the maximal value of the current density is 138× higher than its initial value; see Table 1.

### 3.2. *Null-point with the Positive Pressure Pulse*

In this section, we consider the positive amplitude of the initial pressure pulse, $A_p = +1$. In Figure 7, we present the evolution of mass density and compare it to the already discussed case of $A_p = -0.75$. At the beginning phase of the system evolution, we see that fast and slow magnetoacoustic waves are triggered by the initial pressure pulse. After their escape from the launching place, the entropy wave is formed similarly as in the case of $A_p < 0$. However, contrary to the case of $A_p = -0.75$, its mass density is decreased and temperature enhanced; see Figure 4, right panel. Thus, the positive pressure pulse results in the entropy wave (blob) moving up from (≈20 s), owing to its mass density which is lower than that in the ambient medium. Between (100–200 s) we can observe again the growth of RT instability, similarly as in the previous case. Note that at $t \approx 370$ s the central part of the mass density blob starts to move down due to the gravity and magnetic tension force. The latter plays a role as the magnetic field lines are frozen in the plasma.

Figure 8 shows the time evolution of the mass density in different detection points. In the left panel of this figure, the results for two detection points (center of magnetic null-point, $y = 15.0$ Mm, green line and ($y = 14.8$ Mm), blue line) are presented. Here we can see that in the center of the magnetic null-point the mass density abruptly falls off due to the initial pressure pulse. After a few seconds (1–10 s) the mass density starts to increase in agreement with the theory of the entropy wave. In the meantime, the mass density represented by the blue line starts to relax to its initial equilibrium value. In the right panel of this figure, we show the mass density evolution

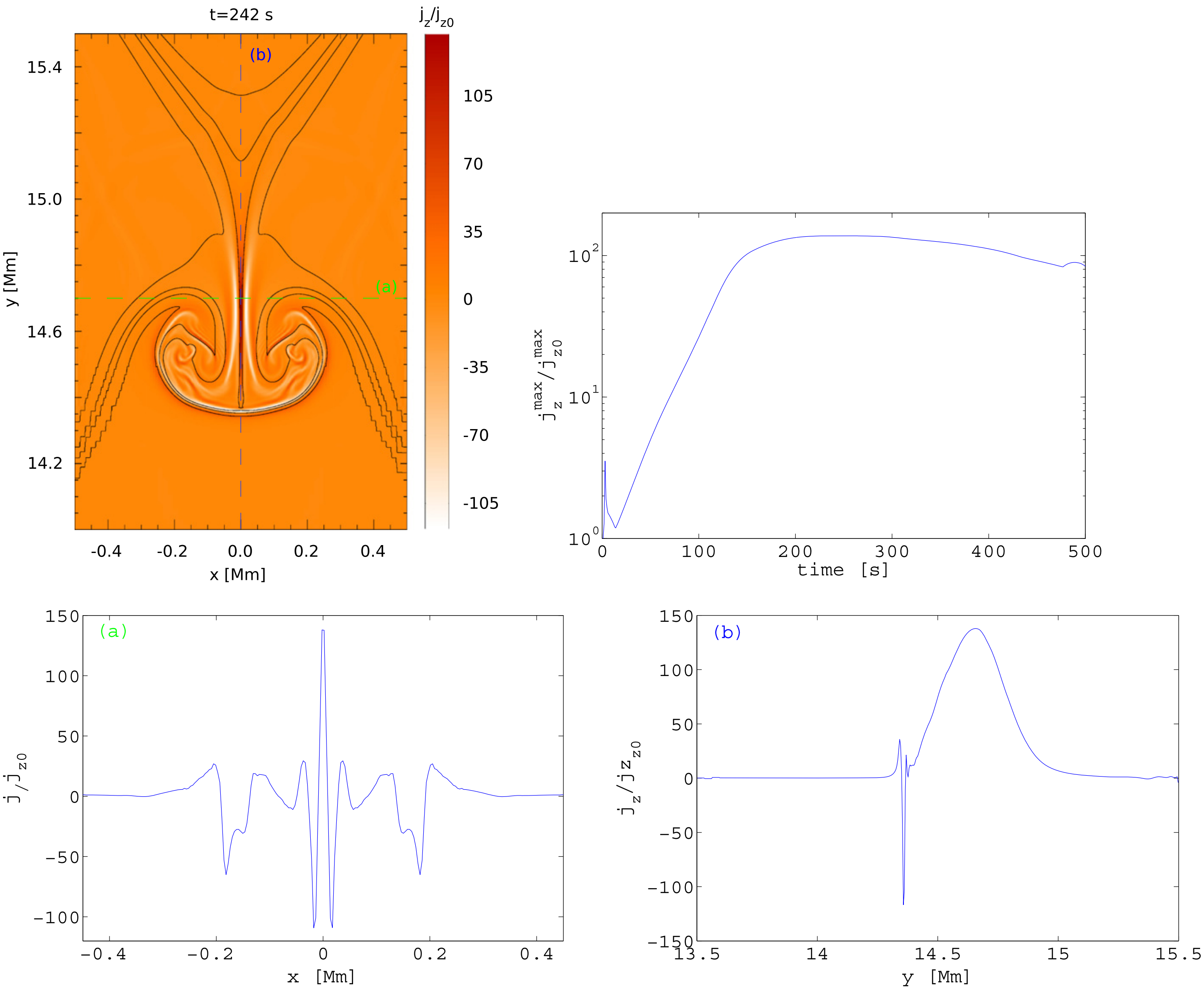


**Figure 6.** Current density for the negative amplitude of the pressure pulse, $A_p = -0.75$, at the time when the current density reached its maximum value, $t^{max} = 242$ s (upper left). The black solid lines show the representative magnetic field lines. The light-green and light-blue dashed lines represent the positions of horizontal and vertical slices (shown in the bottom panels of the figure), respectively. The time evolution of maximum values of the current density (upper right); note that the vertical axis is in the logarithmic scale. The horizontal ($y = 14.65$ Mm) and vertical ($x = 0$ Mm) slices for the maximal current density at $t^{max}$ are shown in the lower left and lower right panels, respectively.

**Table 1**
Relative Ratios of Initial Current Densities with Respect to Initial Current Density in Case (b)—Third Column and Relative Ratios of Maximum Current Density with Respect to Their Initial Values—Fourth Column

| Studied Case | $A_p$ | $j_z^0/j_z^0(b)$ | $j_z^{max}/j_z^0$ |
|---|---|---|---|
| (a): $\mathcal{J}_t/\mathcal{J}_z = 1.25$ | $-0.75$ | 1.98 | 106.39 |
| | $+1.00$ | | 213.76 |
| (b): $\mathcal{J}_t/\mathcal{J}_z = 2.50$ | $-0.75$ | 1.00 | 137.88 |
| | $+1.00$ | | 246.26 |
| (c): $\mathcal{J}_t/\mathcal{J}_z = 5.00$ | $-0.75$ | 0.51 | 163.13 |
| | $+1.00$ | | 286.82 |

in three detection points located above the perturbation point ($y = 15.2$, $y = 15.4$ and $y = 15.6$ Mm; red, green, and blue color, respectively). Similarly to the case of the negative pressure pulse, the mass density oscillates as a result of the fast magnetoacoustic waves propagating through the detection points. Later on (depending on the position of the detection point), the large amplitude waves pass and mass density starts to increase to its equilibrium value. We see that after a certain time (again depending on the detection point position) the mass density tends to decrease—this is well represented by the green line, which results from the gravitational force, as the blob starts to move down at time ≈370 s, as described in the previous paragraph.

Figure 9 consists of four panels, similar to Figure 6. The upper-left panel shows the current density at the time when the current density has reached its maximal value, at $t^{max} = 273$ s. From this figure, we can again clearly see that the maximum value of the current density takes place in the vicinity of the vertical axis of the null-point. For the same reason as in the case of $A_p = -0.75$, the plasma velocity also attains its maximum at this time.

The upper right panel of Figure 9 presents the same quantity using the same scale as in the previous case of the negative pressure pulse. In this figure are two similarly discernible

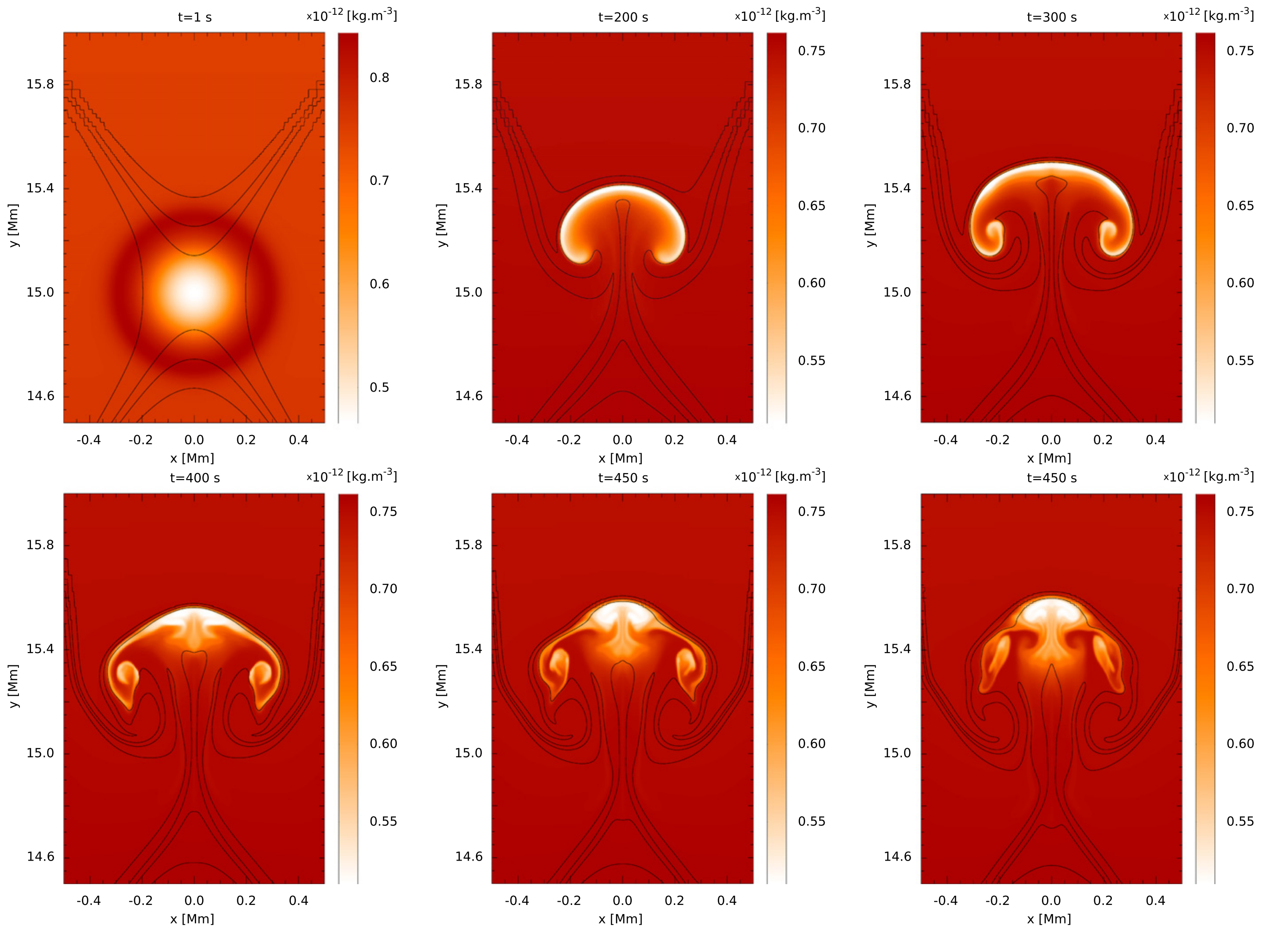


**Figure 7.** Time evolution of mass density for the positive pressure pulse, $A_p = +1$, with a clear development of Rayleigh–Taylor instability. The black solid lines show representative magnetic field lines.

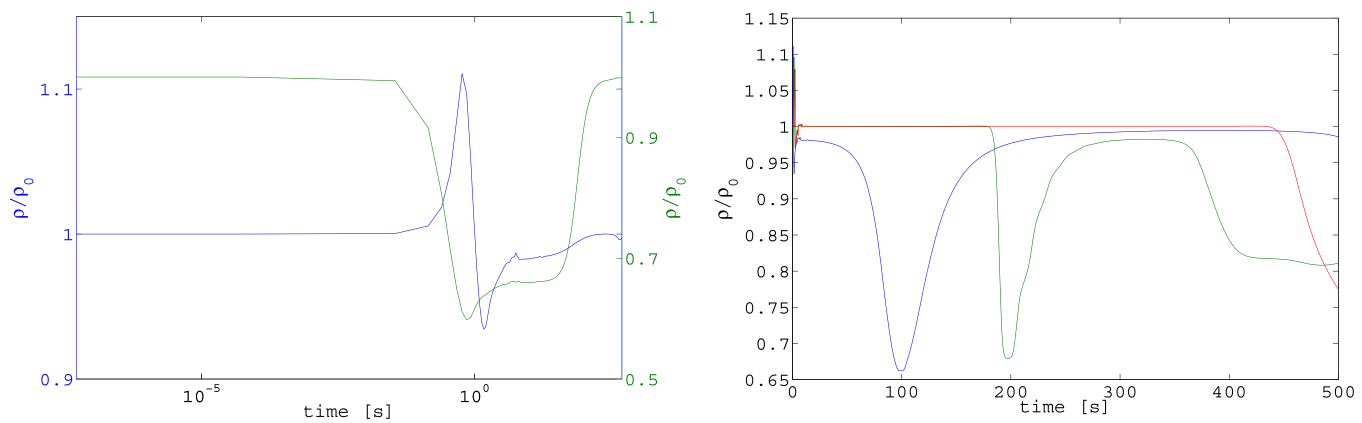


**Figure 8.** Time evolution of mass density, for the positive amplitude of the pressure pulse, $A_p = +1$, in the detection points placed along the $y$ axis, for $x = 0$ Mm, at $y = 14.8$ (left blue line) and $y = 15.0$ Mm (left green line) and $y = 15.2$, $y = 15.4$ and $y = 15.6$ Mm (right red, green and blue line, respectively). Note that the time axis in the left panel is in the logarithmic scale, showing the initial phase of the process.

maxima. However, comparing the results to the first studied case, some differences can be spotted. The first maximum is not related to the increased mass density in the center of the null-point due to the initial pressure pulse. Because the pressure pulse is positive, the mass density in the launching point (center of the magnetic null-point) decreases very quickly. On the other hand, in the vicinity of the perturbation point the mass density increases, as can be seen from Figure 8. After this first maximum, the current density starts to decrease, to the time (30–40 s), when, by the same reason as in the previous case, its growth in time is again evident.

Finally, the two bottom panels of Figure 9 (left and right) show the horizontal and vertical slices, respectively. The horizontal slice has been taken at the point of the maximal

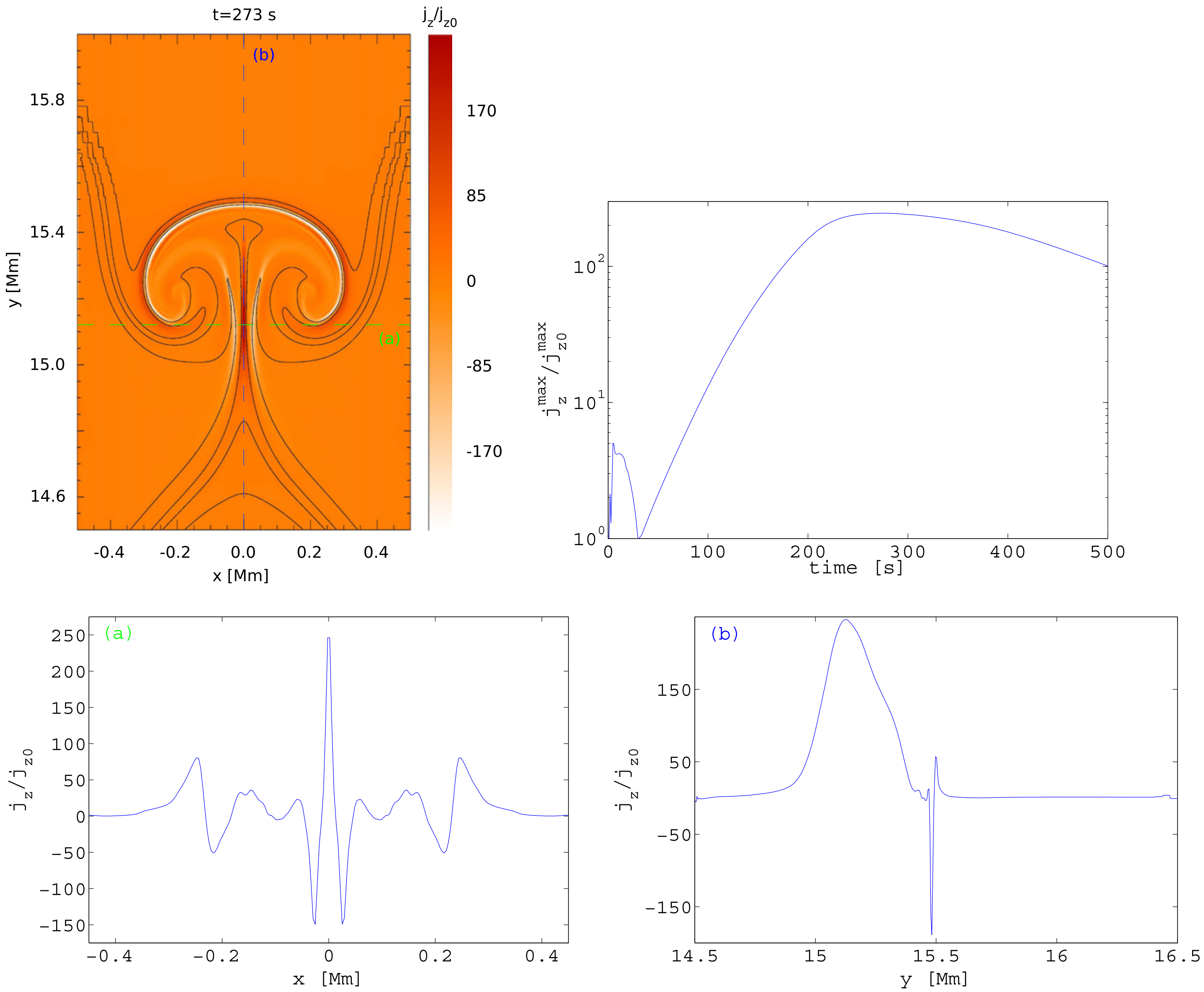


**Figure 9.** Current density for the positive amplitude of the pressure pulse, $A_p = +1$, at the time when the current density reached its maximum $t^{\max} = 273$ s (upper left). The black solid lines show the representative magnetic field lines. The light-green and light-blue dashed lines represent the positions of horizontal and vertical slices (shown in the lower panels of the figure), respectively. The time evolution of maximum values of the current density (upper right); note that the vertical axis is in the logarithmic scale. The horizontal ($y = 15.12$ Mm) and vertical ($x = 0$ Mm) slices for the maximal current density at $t^{\max}$ are shown in the lower left and lower right panels, respectively.

value of the electric current density, i.e., ($x = \langle -0.5, 0.5\rangle$ and $y = 15.12$). The vertical slice is shown along the axis of the null-point, i.e., ($x = 0$ and $y = \langle 14.5, 16.5\rangle$). From both panels, and finally also from the upper right panel, we can see that the maximal value of the current density is 246× higher compared with the initial value; see Table 1.

### 3.3. Comparison of Results for Different Ratios of $\mathcal{J}_t$ and $\mathcal{J}_z$

As we mentioned above, we also numerically studied the following two cases: (a) $\mathcal{J}_t/\mathcal{J}_z = 1.25$ and (c) $\mathcal{J}_t/\mathcal{J}_z = 5.0$. Here we compare these results with case (b): $\mathcal{J}_t/\mathcal{J}_z = 2.5$, described above in more detail.

We found that the evolution of mass density for the cases (a) and (c) exhibits essentially the same behavior as in the case of (b)—corresponding Figures 3 and 7. For this reason, the mass density evolution in the selected detection points (corresponding to Figures 5 and 8) also exhibits practically non-essential changes.

On the other hand, we find interesting changes in current densities for all studied cases; see Table 1. Here we present the relative ratios of initial current densities with respect to the initial current density in case (b)—third column, and relative ratios of maximum current density with respect to their initial values—fourth column. This table reveals that by increasing the parameter $\mathcal{J}_t/\mathcal{J}_z$, the initial current density in the non-potential null point increases. It is expected that if we combine Equations (6) and (12), we can find that the current density is directly proportional to $\mathcal{J}_z$ as

$$j_z = \frac{B_0}{2\mu_0}\mathcal{J}_z. \tag{19}$$

On the other hand, if we compare the values of maximal current densities, we observe that with increasing $\mathcal{J}_t/\mathcal{J}_z$, the maximal current density also increases, for both amplitudes of initial pressure pulses. It is also clearly visible that for the positive pressure pulse ($A_p = +1.0$), the maximum current density is higher than for the negative pressure pulse ($A_p = -0.75$).

**Table 2**
The Times When the Current Density Reached a Maximum Value

| Studied Case | $A_p$ | $t\,(j_z^{\max})$(s) |
|---|---|---|
| (a): $\mathcal{J}_t/\mathcal{J}_z = 1.25$ | $-0.75$ | 242.0 |
| | $+1.00$ | 301.0 |
| (b): $\mathcal{J}_t/\mathcal{J}_z = 2.50$ | $-0.75$ | 242.0 |
| | $+1.00$ | 273.0 |
| (c): $\mathcal{J}_t/\mathcal{J}_z = 5.00$ | $-0.75$ | 244.0 |
| | $+1.00$ | 259.0 |

In Table 2, we present the times at which the current density for all of the studied cases reaches its maximum. We can see that, whereas for the negative initial pulse ($A_p = -0.75$) the time remains practically the same, in the case of the positive pressure pulse ($A_p = +1$), the maximum is reached earlier for a higher value of $\mathcal{J}_t/\mathcal{J}_z$. It is also evident that the time is higher for the positive pressure pulse in all of the studied cases.

## 4. SUMMARY

We performed numerical simulations of evolution of the entropy wave generated by the pressure pulse in the non-potential magnetic null-point. We solved 2D, time-dependent, ideal MHD equations using the FLASH numerical code, which implements AMR. To make the numerical model more realistic, we considered the initial (VAL-C) temperature profile in the gravitationally stratified solar atmosphere. Numerical calculations are performed for three different initial cases. We described here only one case in detail, whereas the remaining two are only quantitatively compared with the first one.

Our results can be summarized as follows. The initial negative or positive pressure pulse, which mimics a sudden cooling, e.g., produced by the thermal instability or sudden heating caused by some energy release, leads, respectively, to the accumulation or evacuation of plasma at the null-point. In our case, this accumulation or evacuation forms the entropy wave, which evolves due to gravity. The entropy wave, produced by the initial pressure pulse of its negative amplitude, leads to a mass density that is greater than in the ambient atmosphere and thus it falls down, being attracted by the gravity. In the case of the positive pressure pulse, the entropy wave propagates upward. These entropy wave motions in both cases are limited by the magnetic tension force.

We found that during an evolution of the entropy wave the electric current is strongly filamented owing to the Rayleigh–Taylor instability. At some locations, the electric current density increases up to 138 times (negative initial pressure pulse) and 246 times (positive pressure pulse) its initial value.

When the current density exceeds the corresponding thresholds for some plasma instabilities (e.g., the ion-acoustic or Buneman instability), then plasma waves can be generated and anomalous resistivity is produced. These processes can release the magnetic field energy through the Ohmic dissipation.

Comparing the numerical results in all of the studied cases, we found that the maximum of the current density ($j_z^{\max}/j_z^0$), reached in the filamentation process, grows with the parameter $\mathcal{J}_t/\mathcal{J}_z$. We also found that for the positive pressure pulses, the current density reached values higher than for the negative pressure pulses.

Based on these results, the following sequence of processes can be proposed. The thermal instability in the non-potential magnetic null-point produces the "catastrophic" cooling, i.e., the negative pressure pulse. This pulse generates the entropy wave and then after its evolution and filamentation process, at locations with highly enhanced electric current densities, the magnetic-energy release (nanoflare) takes place. For example, the bright points in coronal EUV lines (Madjarska et al. 2003; Tian et al. 2008) could be explained by this.

The authors thank the anonymous referee for constructive comments that improved the paper. The authors also acknowledge the Marie Curie FP7-PIRSES-GA-2011-295272 Radio-Sun project. P.J. and M.K. acknowledge support from grants P209/12/0103 of the Grant Agency of the Czech Republic, and the European grant FP7-SPACE-2013–1 F-CHROMA (No. 606862). P.J. thanks Dr. Tom Van Doorsselaere for support of his scientific stay at the Faculty of Science, Catholic University in Leuven, Belgium, during March–May 2015, where P.J. almost finished this work. This work has been supported by a Marie Curie International Research Staff Exchange Scheme Fellowship within the 7th European Community Framework Program and by the Polish National Foundation grant No. 2014/15/B/ST9/00106. The FLASH code used in this work was developed by the DOE-supported ASC/Alliances Center for Astrophysical Thermonuclear Flashes at the University of Chicago.

## REFERENCES

Bárta, M., Büchner, J., Karlický, M., & Skála, J. 2011, ApJ, 737, 24
Chung, T. J. 2002, Computational Fluid Dynamics (New York: Cambridge Univ. Press)
De Moortel, I., & Hood, A. W. 2003, A&A, 408, 755
De Moortel, I., & Nakariakov, V. M. 2012, RSPTA, 370, 3193
Field, G. B. 1965, ApJ, 142, 531
Foullon, C., Verwichte, E., Nakariakov, V. M., & Fletcher, L. 2005, A&A, 440, L59
Fryxell, B., Olson, K., Ricker, P., et al. 2000, ApJS, 131, 273
Goedbloed, J. P. H., & Poedts, S. 2004, Principles of Magnetohydrodynamics (New York: Cambridge Univ. Press)
Jelínek, P., & Karlický, M. 2012, A&A, 537, A46
Jelínek, P., Karlický, M., & Murawski, K. 2012, A&A, 546, A49
Jelínek, P., & Murawski, K. 2013, MNRAS, 434, 2347
Kuźma, B., Murawski, K., & Solov'ev, A. 2015, A&A, 577, A138
Lee, D., & Deane, A. E. 2009, JCoPh, 228, 952
Macnamara, C. K., & Roberts, B. 2010, A&A, 515, A41
Madjarska, M. S., Doyle, J. G., Teriaca, L., & Banerjee, D. 2003, A&A, 398, 775
Mészárosová, H., Karlický, M., Jelínek, P., & Rybák, J. 2014, ApJ, 788, 44
Murawski, K., Zaqarashvili, T. V., & Nakariakov, V. M. 2011, A&A, 533, A18
Nakariakov, V. M., Foullon, C., Verwichte, E., & Young, N. P. 2006, A&A, 452, 343
Nickeler, D. H., Karlický, M., Wiegelmann, T., & Kraus, M. 2013, A&A, 556, A61
Nisticò, G., Nakariakov, V. M., & Verwichte, E. 2013, A&A, 552, A57
Nisticò, G., Pascoe, D. J., & Nakariakov, V. M. 2014, A&A, 569, A12
Parnell, C. E., Neukirch, T., Smith, J. M., & Priest, E. R. 1997, GApFD, 84, 245
Pascoe, D. J. 2014, RAA, 14, 805
Pascoe, D. J., Nakariakov, V. M., & Kupriyanova, E. G. 2013, A&A, 560, A97
Pascoe, D. J., Nakariakov, V. M., & Kupriyanova, E. G. 2014, A&A, 568, A20
Priest, E. R. 1982, Solar Magneto-hydrodynamics (Dordrecht: Reidel)
Solov'ev, A. A. 2010, ARep, 54, 86
Somov, B. V. 2012, in Plasma Astrophysics, Part I, Fundamentals and Practice, Vol. 391 (New York: Springer)
Tian, H., Curdt, W., Marsch, E., & He, J. 2008, ApJL, 681, L121
Toro, E. F. 2006, IJNMF, 52, 433
Vernazza, J. E., Avrett, E. H., & Loeser, R. 1981, ApJS, 45, 635